aerospace

MDPI

Article

3D Turbulent Boundary Layer Separation Control by Multi-Discharge Plasma Actuator

Sergey Chernyshev, Gadzhi Gadzhimagomedov, Aleksandr Kuryachiy, Dmitry Sboev and Stepan Tolkachev *

Central Aerohydrodynamic Institute (TsAGI), 1 Zhukovsky St., Zhukovsky 140180, Russia; slc@tsagi.ru (S.C.); gadji_@mail.ru (G.G.); aleksandr.kuryachiy@tsagi.ru (A.K.); t124@inbox.ru (D.S.)
* Correspondence: tolkachevst@gmail.com; Tel.: +7-915-136-3300

Abstract: In a subsonic wind tunnel, a three-dimensional separation of a developed turbulent boundary layer was simulated on a swept wing flap model. A multi-discharge plasma actuator operating on the basis of dielectric barrier discharge was used to overcome the positive pressure gradient, leading to a three-dimensional separation, when the ultimate streamline on the aerodynamic surface turns along the flap trailing edge. The actuator created an extended streamwise region of volume force, leading to flow acceleration near a streamlined surface. The influence of the force impact direction relative to the flap trailing edge was studied. The experiments demonstrated that the plasma actuator can significantly influence the flow structure in the separation region, leading to a decrease in both the transverse size of the viscous wake behind the flap and the total pressure losses within it.

Keywords: wind tunnel experiment; trailing-edge flap model; turbulent boundary layer; three-dimensional separation; multi-discharge plasma actuator; particle image velocimetry; Pitot comb

Citation: Chernyshev, S.; Gadzhimagomedov, G.; Kuryachiy, A.; Sboev, D.; Tolkachev, S. 3D Turbulent Boundary Layer Separation Control by Multi-Discharge Plasma Actuator. *Aerospace* **2023**, *10*, 869. https://doi.org/10.3390/aerospace10100869

Academic Editor: Kung-Ming Chung

Received: 6 July 2023
Revised: 3 September 2023
Accepted: 8 September 2023
Published: 6 October 2023

1. Introduction

Controlling the boundary layer separation on aircraft lift surfaces is one of the topical issues in applied aerodynamics. It is especially important to increase the aircraft's aerodynamic efficiency during takeoff and landing, when the air flows around a swept high-lift wing at high angles of attack. Boundary layer separation control techniques can be divided into two groups—passive methods, which do not require energy input for control devices, and active ones, which do. Well-known active separation control techniques are boundary layer suction, near-surface jet injection, and moving surfaces. Comparative analysis of various actuators for active flow control is presented, for example, in the review in [1]. In recent years, considerable attention has been paid to plasma actuators, in which near-surface electric discharges of various types are used to create a volume force action on gas flows. The dielectric barrier discharge (DBD) is the most widespread. The main advantages of DBD-actuators are their structural simplicity without moving parts, insignificant dimensions and weight, short response time, and the possibility of being installed flush to a streamlined surface. Descriptions of the physics of volumetric force formation of DBD plasma actuators can be found, for example, in [2,3].

It follows from the reviews of aerodynamic applications of plasma actuators [1,3–8] that the majority of experimental studies is devoted to the problem of boundary layer separation control [9]. In most of these experiments, the flow around a straight wing and the separation control of a laminar boundary layer that occurs near its leading edge were studied. The flow was usually controlled by one or (much less often) several actuators of classical two-electrode design [10]. A recent short review of both numerical and experimental studies on plasma actuators' impact on turbulent boundary layer separation on a straight wing can be found in [11].

Most research is devoted to boundary layer separation on a swept wing. In the experiment cited in [12], the control of global separation of the laminar boundary layer that occurs near the leading edge of the swept wing model at high angles of attack was also studied using a single actuator installed in front of the separation region. A significant shift of the separation region downstream was achieved due to boundary layer turbulization.

It is emphasized in [13] that the effects of plasma actuators on lift enhancement on a swept wing are quite different as compared to on a straight wing. An experimental study was conducted on the flow control over a NACA 65A005 swept wing model using a single plasma actuator setting near the apex in order to manipulate the leading edge vortices in the post-stall regime. It was shown that the change in the intensity of streamwise vortex due to actuator impact led to the lift enhancement [13]. Because of the weaker manifestation of actuators' impact on three-dimensional flow, the increase in the lift coefficient in the case of a swept wing is one order of magnitude smaller than that in typical two-dimensional flow controls on rectangular wings [14].

An experimental study of flow separation control on a 15° swept wing model with NACA0015 airfoil as its section was performed at a flow velocity up to 40 m/s in [15]. In order to reveal the boundary layer separation characteristic and then define the actuator location, preliminary numerical simulation for base flow was carried out. Calculations of the 3D turbulent boundary layer flow using a k-ω model of turbulence demonstrated three-dimensional separation near the wing trailing edge at a high enough (α = 10°) angle of attack. The performances regarding separation flow control of the three types of actuators with plane and saw-toothed exposed electrodes were compared in wind tunnel experiments. The experiments demonstrated that plasma actuator are able to improve the aerodynamic performance of the swept wing when excited at the leading edge.

The experiments with a wing-body configuration model carried out in [16] demonstrated that the effective mechanism for turbulent separation control by the plasma actuator placed at 1% of the chord from the leading edge of the 25° swept wing was to induce the vortex near the wing surface, which could create a relatively large scale disturbance and promote momentum mixing between low-speed flow and main flow regions.

A feature of the experiments presented below is the study of the possibility of controlling the developed turbulent boundary layer separation in the vicinity of the swept wing flap trailing edge. Three-dimensional separation is under consideration when the limiting streamline on the aerodynamic surface, the direction of which is determined by the skin friction force vector, takes the direction along the trailing edge under the action of an adverse longitudinal pressure gradient. The main distinction of the present experiments is a consideration of the force impact distributed directly before and inside the separation region, but not near the wing's leading edge, as in most of the previous studies.

Boundary layer separation control using plasma actuators is based on overcoming an unfavorable pressure gradient by introducing additional momentum into the near-wall flow region in the boundary layer. An additional impulse can be introduced directly due to the volume force directed along the pressure gradient, when the external electrodes of the actuators are located along the wingspan. This method is typically used to control laminar boundary layer separation. The second way to overcome an unfavorable pressure gradient, used to control the turbulent boundary layer separation, is based on the momentum exchange between a high-speed flow in the outer part of the layer and a low-speed flow in its near-wall region. In this case, the actuator electrodes are spaced some distance apart along the external flow. As a result of force action by the actuators, longitudinal oppositely rotating vortex couples are formed. These vortices provide a momentum exchange between the outer and near-wall regions of the turbulent boundary layer. This leads to an increase in the vertical gradient of the longitudinal velocity component on the aerodynamic surface and a downstream shift of the boundary layer separation line [17].

Taking into account that in the vicinity of the three-dimensional separation, the components of the longitudinal and transverse velocities in the boundary layer are commensurable and the streamlines are strongly curved, it is difficult to determine the location of the actuators that would provide an efficient momentum exchange inside the layer. Therefore, in the present experiments, the first method of introducing momentum into the turbulent boundary layer using a volume force action directed predominantly along the longitudinal pressure gradient was used.

2. Multi-Discharge Actuator

A volume-unidirectional force acting upon the streamwise aerodynamic surface area was generated by multi-discharge plasma actuators of varying design complexity [18–22]. A multi-discharge actuator (MDA) was developed [23], the main advantages of which, over the known schemes, are the simplicity of the design and the possibility of significant miniaturization, that is, reducing the gap between adjacent actuators [24]. The MDA design with indication of the internal dimensions (mm) is shown in Figure 1a, and the external dimensions of the model are shown (mm) in Figure 1b.

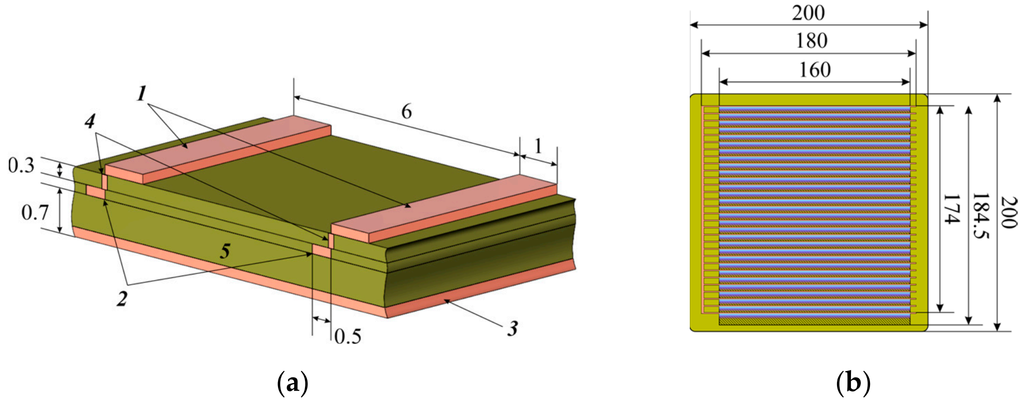

Figure 1. Multi-discharge actuator design (**a**) and model dimensions (**b**): electrodes: 1—external, 2—shielding, 3—accelerating; 4—shunts, 5—dielectric layers.

The external *1* and shielding *2* electrodes were made in the form of a set (comb) of parallel conductors with constant spacing and were electrically connected using metal shunts *4* on the common base of the comb shown on the left side of Figure 1b. An alternating voltage was applied to electrodes *1* and *2*. Solid accelerating electrode *3* was grounded. Electrodes *1*–*3* were separated by two dielectric layers *5*. Due to the equipotentiality of electrodes *1* and *2*, the electric field strength near the left (passive) edges of the external electrodes was significantly weakened, and dielectric barrier discharge (DBD) occurred only in the vicinity of the right (active) edges, where the influence of the shielding electrodes was insignificant. The time-averaged horizontal component of the volume force was directed from the active edges from left to right and accelerated the gas in this direction over the entire MDA surface.

The MDA model used in the experiments had 30 pairs of copper electrodes. The dielectric layers are made of fiberglass. The model was powered by a negative saw-tooth voltage source at a fixed frequency of 12 kHz and an amplitude in the range from E = 4.5 kV (peak-to-peak voltage E_{pp} = 9 kV), when the discharge becomes sufficiently uniform along the electrodes, to E = 8 kV, and a dielectric breakdown occurred during the experiments. Figure 2 shows photographs of the discharge at two voltage amplitude values. It can be seen that the discharge burns only at the lower edges of the external electrodes, and at a voltage amplitude above ±5 kV, the discharge glow covers most of the gaps between the electrodes.

It should be noted that two MDA models made according to Figure 1a with electrode spacing of 5 and 7 mm were successfully used in the experiments investigating control of the crossflow stability in a 3D laminar boundary layer [25].

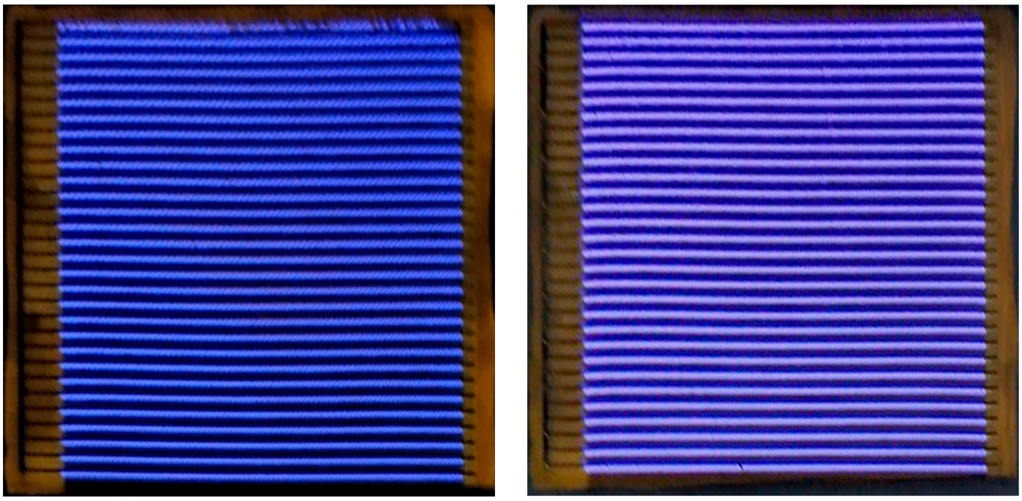

(a) (b)

Figure 2. DBD on MDA at voltage amplitudes of ±4.5 kV (**a**) and ±5 kV (**b**).

3. Experimental Procedure in a Wind Tunnel

Experiments on control of the turbulent boundary layer separation on a swept flap model were carried out in the TsAGI T-03 wind tunnel, which was equipped with an Eiffel chamber. The free stream velocity varied in the range of 8 to 36 m/s. During the experiments, the air temperature, as well as the pressure in the settling chamber and in the control section immediately at the contractor outlet, were measured. This made it possible to control the free stream velocity with an accuracy of about 1%. At the contractor exit, a flow core was formed with a width of 580 mm, a height of 370 mm, and a length of 1300 mm. The level of free stream turbulence typical of a wind tunnel with an empty test section is about Tu = 0.35%.

The prototype of the model in this paper was the configuration used to study the three-dimensional turbulent boundary layer and its separation in [26]. As a wing flap model, a swept flat plate with a sweep angle of 35°, made of 15 mm thick plexiglass, was used. The profile of the leading and trailing edges was cylindrical, with a radius of 7.5 mm. The main dimensions of the model are shown in Figure 3. The model was equipped with a seat for installing a replaceable ring plate (rotating insert) with a diameter of 340 mm, which allowed us to change the direction of the MDA force action on the boundary layer. The center of the insert was located at a distance of 363.6 mm from the leading edge of the model. Two ring plates were manufactured. One ring plate was designed to measure the pressure distribution over the model and was equipped with four pressure taps connected to electronic pressure gauges by a pneumatic line and located at distances of 255.2 mm, 304.4 mm, 356.8 mm, and 435.5 mm along the normal line from the leading edge of the plate. On the model itself, there were four more pressure taps at distances of 103.6 mm, 144.5 mm, 214.1 mm, and 517.3 mm along the normal line from the leading edge. The other ring plate was designed to install the MDA model. On the underside of the model, the gap between the ring insert and the model itself was sealed to avoid undesirable air flow through this gap. On the upper side of the model, the vertical step between the insert and the model did not exceed 0.05 mm.

To visualize the velocity fields in the flow separation region, the POLIS PIV (particle image velocimetry) system was used, both with horizontal and vertical orientations of the laser light sheet. In the horizontal configuration, the laser light sheet was placed parallel to the model surface at a distance of 5 mm from it. In the vertical configuration, the laser light sheet was located perpendicular to the plane of the model and parallel to the free stream velocity. The thickness of the laser light sheet in the measurement area was about 1 mm. The Martin MAGNUM 1800 aerosol generator was used as a source of tracer particles with a characteristic particle size of 1 μm. The source of illumination was the Quantel Twins BSL

140 double-pulse solid-state Nd:YAG laser with a wavelength of 532 nm and a pulse energy of 140 mJ. To register images of tracer particles, the cross-correlation camera Videoscan 4021 (of 2048 × 2048 resolution), with a 60 mm lens, was used. The extent of the region above the model in which the velocity field was measured was about 230 mm. A total of 100 pairs of frames, with a frequency of 1.25 Hz, were recorded on each regime. As a result of using an iterative cross-correlation algorithm with continuous displacement of regions and overlap of calculated regions equal to 50%, instantaneous velocity fields were obtained. The spatial resolution values of the obtained vector fields were 2 × 2 mm and 2.75 × 2.75 mm when measured in the vertical and horizontal planes, respectively. To measure the characteristics of the boundary layer near the aerodynamic surface, a ×2 teleconverter was used, which ultimately gave a focal length of 120 mm. The measuring area was 25 × 25 mm, and the spatial resolution of the vector field was 0.4 mm. To improve the quality of the obtained images and reduce the background illumination, a 532 nm narrowband laser light filter was installed on the lens.

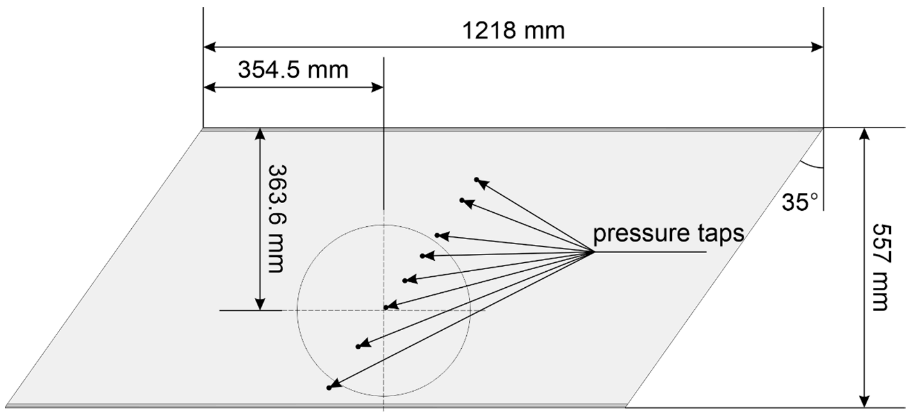

Figure 3. Main dimensions of the flap model.

To measure the flap model wake pressure, a Pitot comb was used. It was equipped with 82 tubes (80 of them are located at a pitch of 2.5 mm), of which 31 tubes (5 mm pitch) were used, connected to a 32-channel container with pressure sensors. The comb was installed at a distance of 30 mm from the trailing edge of the plate in the direction along the free stream velocity.

The registration of pneumometric measurements (including flow parameters, pressure distribution on the surface of the model, and pressure distribution on the Pitot comb) was carried out using multi-channel units with Honeywell XCA515AN pressure sensors calibrated individually at the manufacturing stage. Analog signals from pressure containers were digitized in an 80-channel 16-bit ADC NI PXI-6255 (manufacturer «National Instruments») with a frequency of 2 kHz. The recording time for each mode was 10 s. The average pressure values during the measurement were recorded in the output file.

To create a longitudinal adverse pressure gradient over the plate, a displacement body in the form of an inverted Eppler E662 airfoil was installed. The leading edge of the displacement body was parallel to the leading edge of the plate. A negative angle of attack of the displacement body equal to $-12.4°$ was set to ensure an adverse pressure gradient and favorable conditions for the flow separation onset. In the course of preliminary experiments, it was found that separation occurred on the displacement body. Mounting turbulators on the acceleration part of the displacement body [27] did not lead to the desired results. The solution to this problem was the use of a slat with a chord of 109.4 mm and a thickness of 16.6 mm. The final test configuration is shown in Figure 4a, which indicates the main elements. A general view of the wind tunnel test section with the model, the displacement body, and the Pitot comb is shown in Figure 4b.

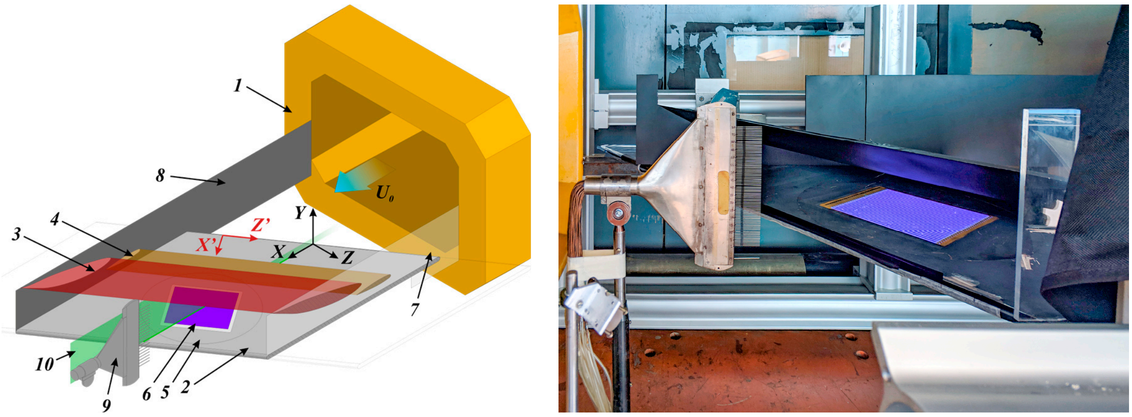

(**a**) (**b**)

Figure 4. Test configuration: scheme (**a**): general view (**b**): 1—contractor exit; 2—flap model; 3—displacement body; 4—slat; 5—replaceable ring plate (rotating insert); 6—MDA; 7—transparent wall; 8—black painted wall; 9—Pitot comb; 10—vertical laser light sheet for PIV.

A coarse-grained sandpaper turbulator was mounted on the leading edge of the swept plate to ensure the development of a turbulent boundary layer in the flow separation region. The minimum distance between the slat and the surface of the plate model was 22 mm. The minimum distance between the displacement body and the plate surface was 45 mm. To minimize the 3D effects, flat walls were installed between the plate and the displacement body. One wall was made of transparent Plexiglas to enable PIV measurements.

The following coordinate systems were used in the experiments: the X-axis was directed along the line of the pressure taps shown in Figure 3 and was measured from the leading edge of the model; the Y-axis was perpendicular to the plane of the model and was measured from its surface; and the Z-axis was perpendicular to the X-axis and was measured from the center of the rotating ring plate. For visual clarity of the PIV measurement results, the Z'-axis was used with the origin in the center of the ring plate, directed along the trailing edge of the model. When studying the influence of the MDA force action direction, the X'-axis was used, which was perpendicular to the leading edge of the model passing through the center of the ring plate. The positive angle of the ring plate rotation, which determines the MDA force action direction, was measured from this axis clockwise, and the negative angle was measured from this axis counterclockwise, as shown in Figure 5, where the blue dashed line symbolizes the limiting streamline on the model surface and the arrows on it indicate the skin friction vector direction.

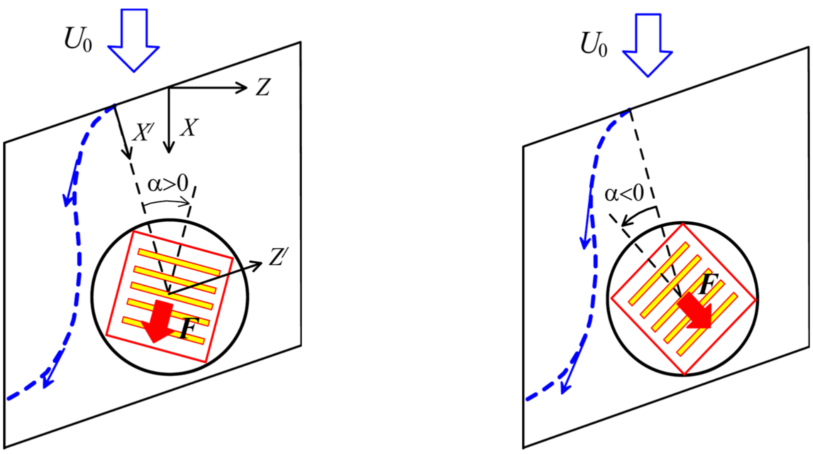

(**a**) (**b**)

Figure 5. Volume force direction F at positive (**a**) and negative (**b**) angles of MDA rotation.

4. Experimental Results

4.1. Characteristics of Turbulent Boundary Layer and 3D Separation Images

The first series of experiments was carried out at a zero angle of rotation of the ring plate on which the MDA was installed. In accordance with Figure 5, this means that the external electrodes of the MDA were parallel to the trailing edge of the plate, and the horizontal component of the volume force action was directed perpendicular to the edge, that is, along the unfavorable pressure gradient.

Longitudinal distributions of the pressure coefficient on the model surface, measured at the pressure taps (Figure 3), are shown in Figure 6 for two values of free stream velocity. In both cases, due to the influence of the displacement body, a positive pressure gradient occurred downstream from X = 260 mm.

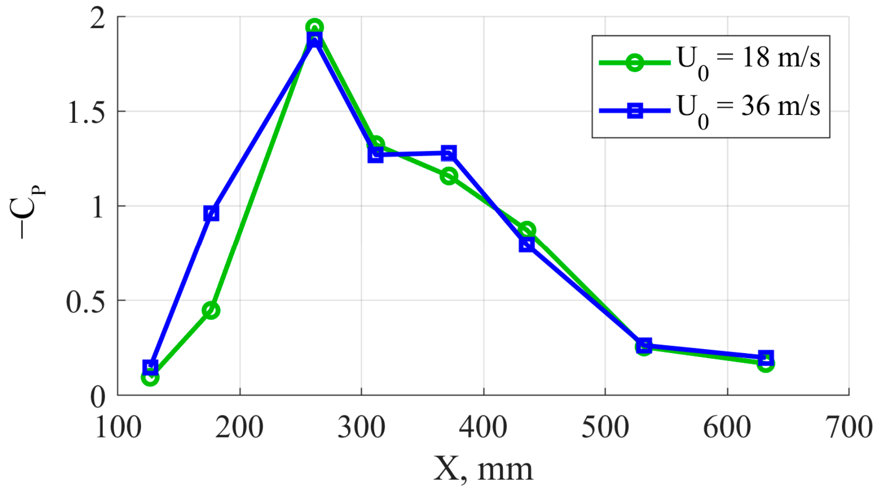

Figure 6. Pressure distributions on a swept flap model.

The flow patterns without the MDA impact, obtained using PIV with a vertical laser light sheet in the X-Y plane at $Z = 0$ for three values of the free stream velocity and presented in Figure 7, confirm that the boundary layer separation occurred on the flap model and not on the displacement body. The flow direction is from left to right. At the top left, a trace is clearly visible, which arose during the flow over the slat. The streamlines corresponding to the reverse flow in the separation region are marked in white.

The flow patterns obtained with a horizontal laser light sheet in the X'-Z' plane at Y = 5 mm are shown in Figure 8. The red line corresponds to U_X = 0 m/s. At the free stream velocity U_0 = 8 m/s, the flow before separation was almost independent of the Z' coordinate, i.e., edge effects due to the side walls did not appear in the measurement area. Some irregularity of the separation line marked in red is associated with errors in PIV measurements of flow velocity. As Figure 8b,c show, the spanwise flow uniformity was perturbed as the free stream velocity increased.

The longitudinal velocity component profiles, measured in the section X = 404 mm upstream of the separation region, are shown in Figure 9 in Clauser coordinates [28]. The main characteristics of the boundary layer at X = 404 mm are given in Table 1, where δ^* is the displacement thickness; θ is the momentum thickness; Re_θ is the Reynolds number calculated from θ and the flow velocity U_e outside the boundary layer; δ_{99} is the boundary layer thickness, corresponding to a velocity of $0.99U_e$; and G is the Clauser shape parameter. The given parameters correspond to a developed turbulent boundary layer. The average velocity profiles approximately correspond to a one-parameter family with the parameter G = 7.2–7.8.

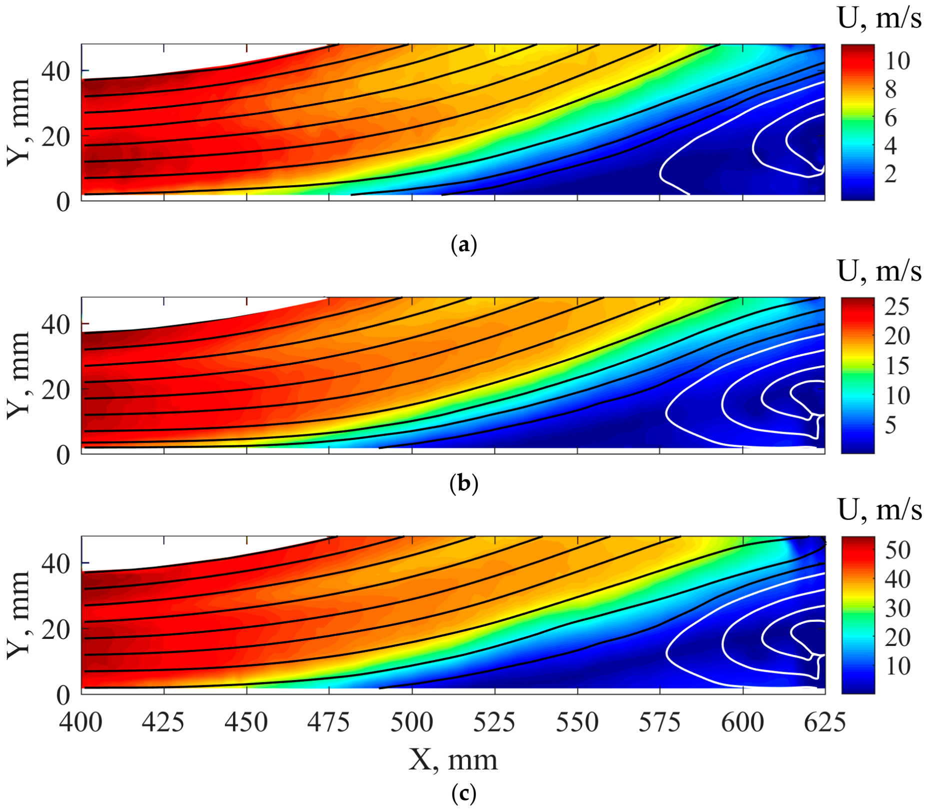

Figure 7. Flow structure (side view) without DBD: (**a**) U_0 = 8 m/s, (**b**) U_0 = 18 m/s, (**c**) U_0 = 36 m/s. The area of the MDA in which the discharge occurs is in the X position between 335 and 548 mm.

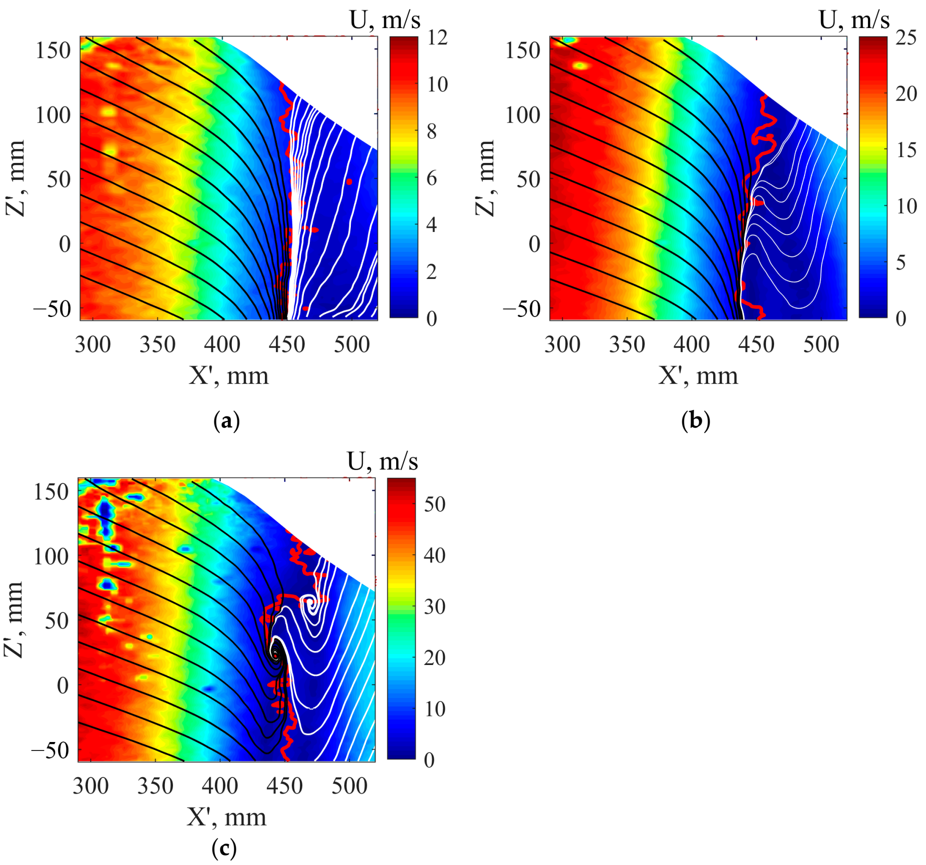

Figure 8. Flow structure (top view) without DBD: (**a**) U_0 = 8 m/s, (**b**) U_0 = 18 m/s, (**c**) U_0 = 36 m/s.

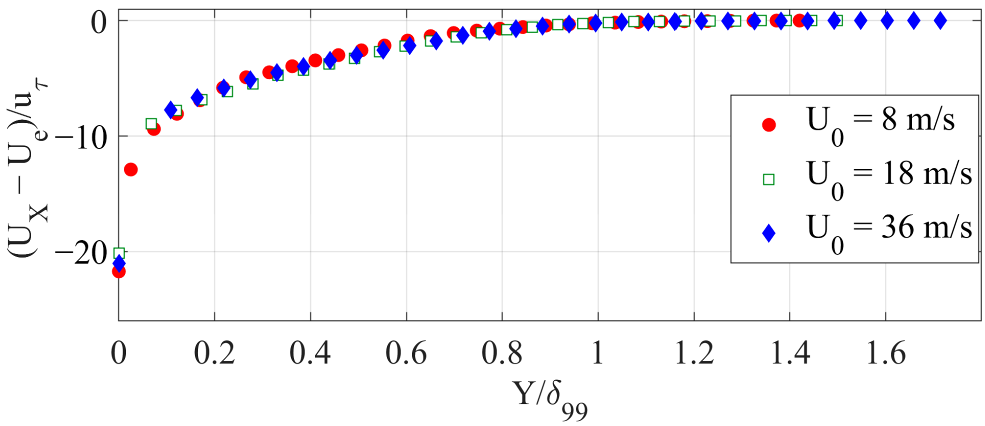

Figure 9. Velocity profiles upstream of separation.

Table 1. Boundary layer characteristics upstream of separation.

U_0, m/s	δ^*, mm	θ, mm	δ_{99}, mm	$H = \delta^*/\theta$	Re_θ	G
8	1.42	0.95	8.33	1.49	671	7.16
18	1.49	0.96	7.56	1.55	1525	7.16
36	1.38	0.87	7.24	1.59	2854	7.81

4.2. MDA Impact at Various Free Stream Velocities

The MDA volume force impact on the three-dimensional separation region location and size can be estimated by the isolines of the longitudinal velocity component U_X, measured using PIV in the vicinity of its zero values $-\Delta U_X \leq U_X \leq \Delta U_X$. These isolines are shown in Figure 10 for three values of free stream velocity and two values of voltage amplitude on MDA. The values of the ranges ΔU_X, as well as estimates of the separation line shift, are given in Table 2.

Table 2. Estimations of MDA impact on separation location.

U_0, m/s	ΔU_X, m/s	$X_{sep\,0}$, mm	X_{sep}, mm		ΔX_{sep}, mm		$\Delta X_{sep}/\delta^*$	
			4.5 kV	5 kV	4.5 kV	5 kV	4.5 kV	5 kV
8	0.025	527	549	557	22	30	15.5	21.1
18	0.05	534	531	528	−3	−6	−2	−4
36	0.1	518	518	518	0	0	0	0

At a low flow velocity, U_0 = 8 m/s, the MDA impact led to a noticeable downstream shift of the separation region onset and an increase in the angle of inclination to the streamlined surface of the separation region boundary (Figure 10a). Increasing the flow velocity to U_0 = 18 m/s resulted in a separation line shift upstream under the MDA impact, and the greater the voltage amplitude on the MDA was, the more significant the shift became (Figure 10b). The separated flow region in the area under consideration also thickened. With a further increase in the flow velocity up to U_0 = 36 m/s, the velocity isolines corresponding to the range indicated in Table 2 practically overlapped each other (Figure 10c).

The profiles of the longitudinal velocity component measured downstream of the separation line near the right boundary of the PIV measurement area at X = 598 mm (see Figure 7), shown in Figure 11, confirm the effect of an increase in the vertical size of the reverse flow region under the impact of MDA, especially at a low free stream velocity.

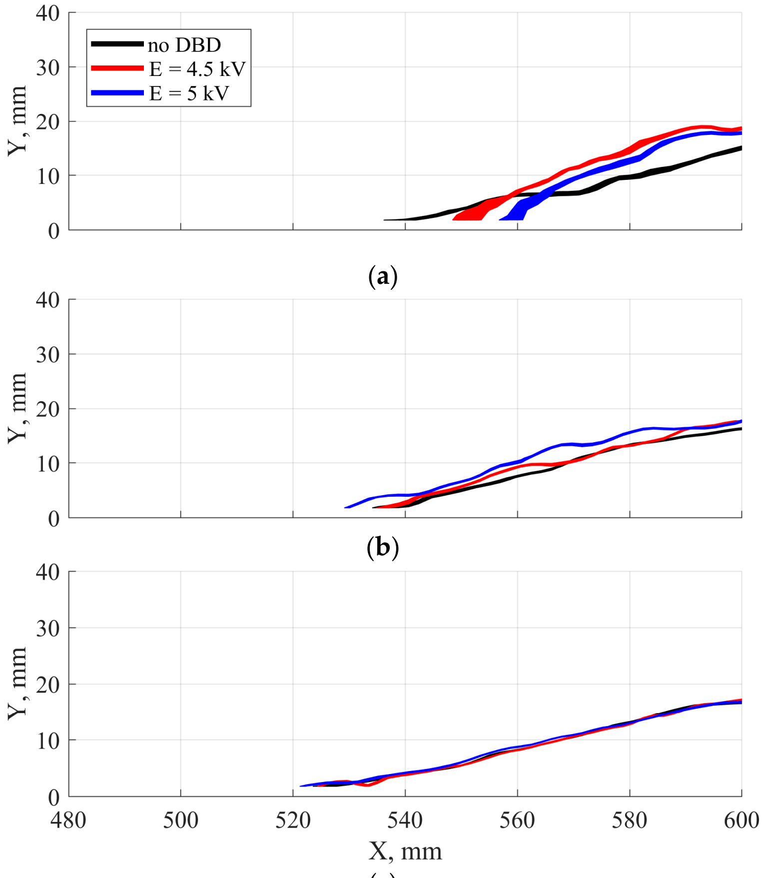

Figure 10. Isolines of streamwise velocity close to zero at free stream velocities of: (**a**) U_0 = 8 m/s, (**b**) U_0 = 18 m/s, (**c**) U_0 = 36 m/s.

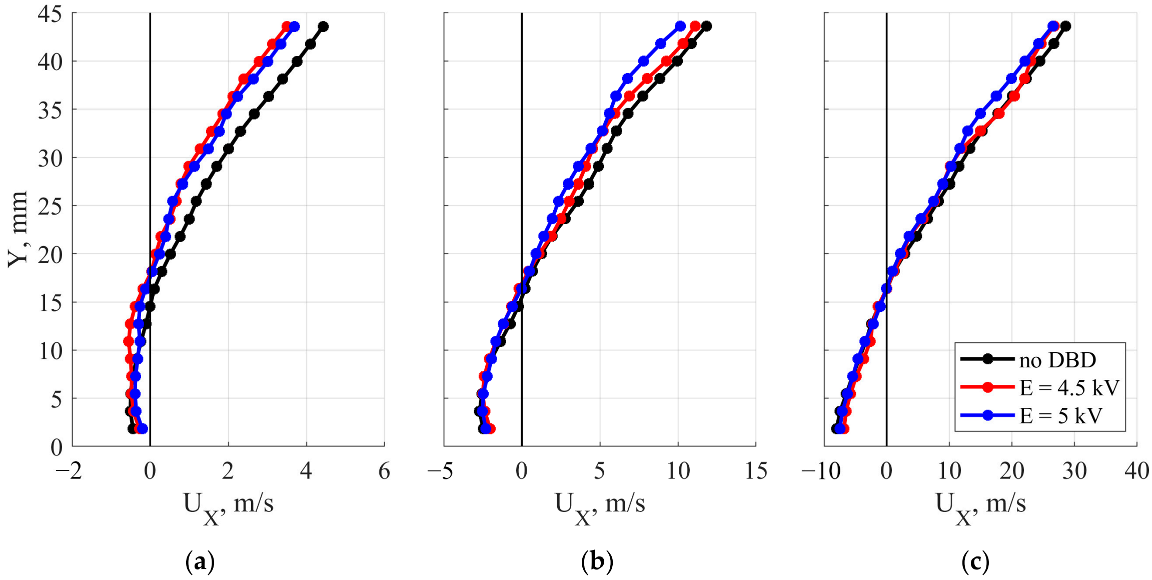

Figure 11. Streamwise velocity distributions in separation region at X = 598 mm at free stream velocities of: (**a**) U_0 = 8 m/s, (**b**) U_0 = 18 m/s, (**c**) U_0 = 36 m/s.

However, vertical distributions of the value $\Delta P = P - P_0$ are shown in Figure 12, where P is the total pressure measured by the comb, P_0 is the total pressure in the control section of the wind tunnel exit nozzle. This clearly demonstrates that the MDA action decreased the vertical size of the model wake due to the three-dimensional separation of the boundary layer. It should be noted that the distance to the trailing edge of the model, measured along the X-axis, which was used in the presentation of data in Figures 7 and 9–11, was $X_{te} = 557/\cos(35°) = 680$ mm (see Figure 3). With regard to the distance between the trailing edge of the model and the comb of pressure taps, which is equal to 30 mm, the distributions of total pressure losses in the wake presented in Figure 12 correspond to the coordinate $X_{Pc} = 710$ mm.

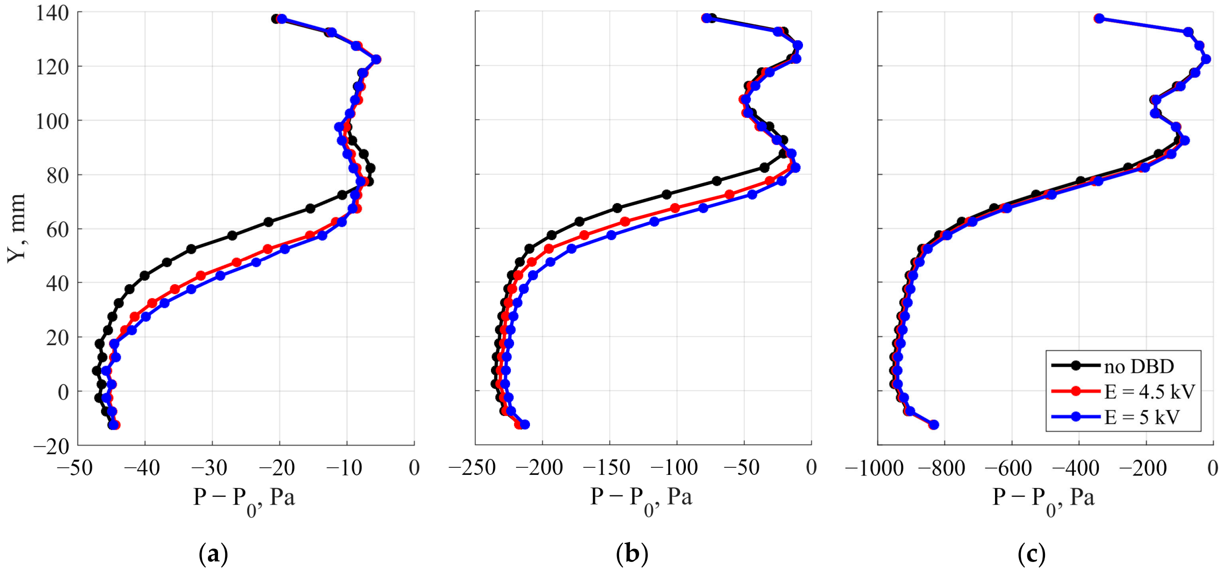

Figure 12. Total pressure losses in separation wake at X = 710 mm at free stream velocities of: (**a**) U_0 = 8 m/s, (**b**) U_0 = 18 m/s, (**c**) U_0 = 36 m/s.

As follows from Figure 12, under the MDA action, not only did the transverse size of the wake area decrease, but the flow momentum loss in it did as well. This is known as streamlined body drag. This favorable effect is enhanced with increasing voltage amplitude on the MDA.

It should be noted that the measurement of the total pressure behind a streamlined body using a Pitot comb is a classical method for estimating the aerodynamic drag of a body. It should be kept in mind that in this case, the distributions of the total pressure (measured by the comb and reference value) difference shown in Figure 12 were due, in part, to the angle between the flow velocity and the Pitot tubes. The second part of the difference may have been due to the pressure drop caused by viscous forces in the channel formed by the flap model and the displacement body.

There are two minima in the presented distributions. The lower minimum corresponds to the wake induced by the boundary layer separation on the model, and the upper one corresponds to the viscous slat wake. For an integral assessment of the effect of MDA on the flow using the pressure distribution measured by the Pitot comb, it is convenient to operate with a specific force value, which makes it possible to estimate the integral loss of flow momentum due to its separation and friction:

$$f = \int_{Y_0}^{Y_s} (P - P_0)\, dY, \tag{1}$$

Here, the upper integration limit Y_s is the value of the vertical coordinate corresponding to the center of the viscous slat wake; $Y_0 = -12.5$ mm is the coordinate of the lowest pressure tap on the comb.

The results, as measured by a Pitot comb, are shown in Table 3, where f_0 is the value of the specific force (1) without the MDA impact. It can be seen that with the increase in the flow velocity, the absolute reduction of momentum loss due to the effect of MDA increased, but the relative reduction decreased. The positive effect of the MDA certainly grew when the amplitude of the DBD voltage increased.

Table 3. Estimations of the flow's total momentum losses.

U_0, m/s	E, kV	$f - f_0$, N/m	$(f - f_0)/f_0$	E, kV	$f - f_0$, N/m	$(f - f_0)/f_0$
8	4.5	−0.46	−0.136	5	−0.5	−0.147
18	4.5	−1.35	−0.07	5	−2.19	−0.114
36	4.5	−2.5	−0.031	5	−2.88	−0.036

4.3. Influence of the Force Impact Direction on Separation

Studies on the effect of rotation angle α of the ring plate, on which the MDA is installed, were carried out at one voltage amplitude, $E = \pm 5$ kV. The experiments were carried out at one negative ($\alpha = -30°$) and two positive ($\alpha = +30°, +60°$) ring plate rotation angles, and the results were compared with the basic mode $\alpha = 0°$, where the MDA force action is directed parallel to the external pressure gradient vector.

In accordance with Figure 5, at a positive angle α, the flow was accelerated not only towards the unfavorable pressure gradient (along the X' axis), but also along the trailing edge of the model in the direction of the skin friction vector. At a negative angle α, the volume force component F_Z, parallel to the trailing edge, decelerated the flow in the near-wall region of the boundary layer in the vicinity of the separation line.

The influence of the direction of the MDA force action on the separation region boundary is shown in Figure 13, which shows the isolines of the streamwise velocity component in the ranges of $-\Delta U_X \leq U_X \leq \Delta U_X$. The boundaries of the ranges ΔU_X for different free stream velocity values are shown in Table 2. Referring to Figure 13, the largest shift in the flow separation point downstream was achieved at a positive angle $\alpha = +30°$ for all considered flow velocity values. In this case, the direction of the volume force vector F differed from the direction of the free stream velocity vector by only 5°. Changes in the location of the separation region relative to the reference case ($\alpha = 0°$) at other MDA rotation angles depended on the free stream velocity.

At a flow velocity of $U_0 = 8$ m/s and an MDA rotation angle of $\alpha = +30°$, the isolines $U_X \approx 0$ m/s had a turning point at a distance of $Y_t \approx 7$ mm from the model surface (see Figure 13a), less than the thickness of the boundary layer before separation: $Y_\delta \approx 10$–11 mm (thickness δ_{99} indicated in Table 1 is usually noticeably smaller than thickness δ). This indicates the formation of a jet-type streamwise velocity profile with a local maximum near the wall in this mode of action.

With an increase in the MDA rotation angle up to $\alpha = +60°$, the separation line almost returned to the position corresponding to $\alpha = 0°$. At the same time, the separation region expanded remarkably at X > 570 mm. At a negative angle of rotation, the component of the flow velocity directed parallel to the trailing edge decelerated due to the MDA impact. As a result of this flow deceleration, the separation region shifted strongly upstream.

At a velocity of $U_0 = 18$ m/s, the earliest separation also occurred at a negative angle, $\alpha = -30°$ (see Figure 13b), but the difference with the reference case was no longer as significant. With a further increase in velocity to $U_0 = 36$ m/s, separation at a positive angle, $\alpha = +60°$, occurred earlier than at a negative angle, $\alpha = -30°$ (see Figure 13c). The ambiguous effect of the MDA's impact on the location and size of the three-dimensional separation region, observed both with a change in the flow velocity and a constant impact angle, $\alpha = 0°$ (Figure 10), as well as with a change in the impact angle and velocity (Figure 13), requires further study and explanation.

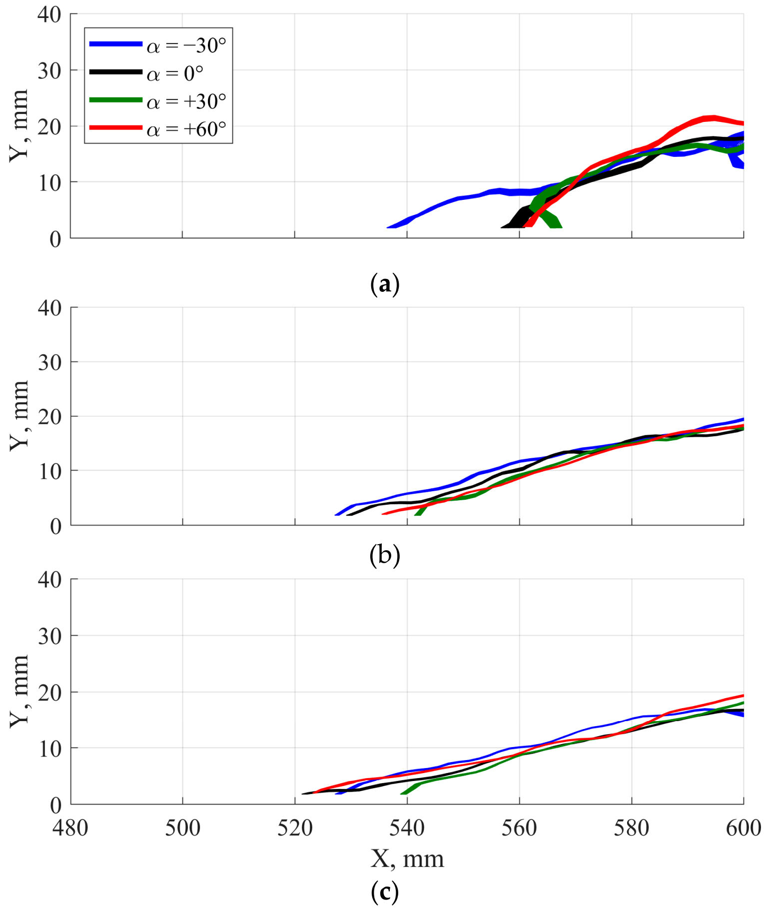

Figure 13. Influence of the MDA rotation angle on the shape of isolines of streamwise velocity close to zero at free stream velocities of: (**a**) U_0 = 8 m/s, (**b**) U_0 = 18 m/s, (**c**) U_0 = 36 m/s.

The distributions of total pressure losses in the swept plate model wake presented in Figure 14a demonstrate that at a flow velocity of U_0 = 8 m/s, the minimum pressure losses occurred at a positive MDA rotation angle, α = +30°, and, quite unexpectedly, at a negative angle, $\alpha = -30°$. For these two MDA rotation angles, the pressure minimum in the slat wake shifted down in the graph (which indicates a smaller size of the separation region), and the value of the total pressure defect was less than that at the α = 0° angle. The greatest pressure losses occurred at a large, positive angle, α = +60°. At the free stream velocity of U_0 = 18 m/s, the zero MDA rotation angle was optimal (Figure 14b), and the greatest pressure losses, as in the case of U_0 = 8 m/s, occurred at the angle of α = +60°. With a further increase in velocity to U_0 = 36 m/s, there was, again, a favorable effect of positive MDA rotation angles. At a negative angle of $\alpha = -30°$, the pressure losses increased. The conclusions drawn are illustrated in Figure 15, which shows the dependences of the change in the specific force f, estimated by the Equation (1), and characterizes the integral loss of the flow momentum on the MDA rotation angle compared with $f_{\alpha 0}$, which is the specific force achieved at α = 0°.

4.4. Influence of the Voltage Increase on Separation

Experiments were carried out at the maximum possible power supply voltage amplitude for this MDA model in order to implement a greater effect on the flow. The free stream flow velocity was U_0 = 18 m/s. This mode was chosen as a trade-off when the free stream flow velocity was sufficiently high and the MDA effect on the flow separation was noticeable in the experiments described above. The MDA rotation angle α = 0° was also fixed. The maximum applied voltage amplitude, which ensures a sufficiently uniform stable discharge burning, was $E = \pm 7.5$ kV. With a further increase in voltage, the uniform structure of the discharge was perturbed: additional discharges appeared on the shielding electrodes, filling the gaps between the external electrodes, and thus disrupting the force action in one direction. When the voltage $E = \pm 8$ kV was applied, the actuator quickly failed as a result of electrical breakdown (Figure 16); however, the necessary data were obtained using PIV measurements and a Pitot comb prior to that.

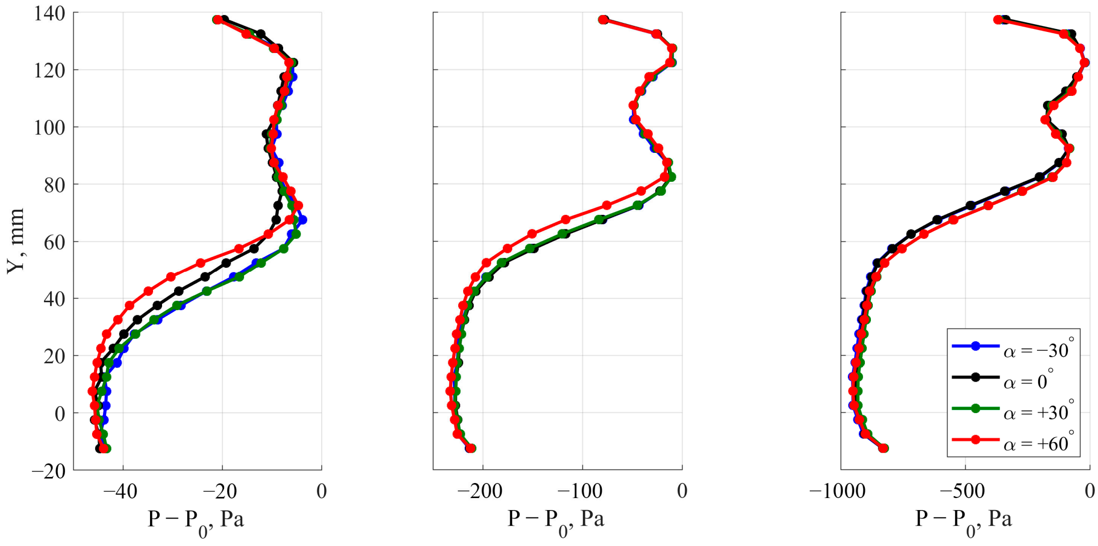

(**a**) (**b**) (**c**)

Figure 14. Influence of the MDA rotation angle on total pressure losses in separation wake at X = 710 mm at free stream velocities of: (**a**) $U_0 = 8$ m/s, (**b**) $U_0 = 18$ m/s, (**c**) $U_0 = 36$ m/s.

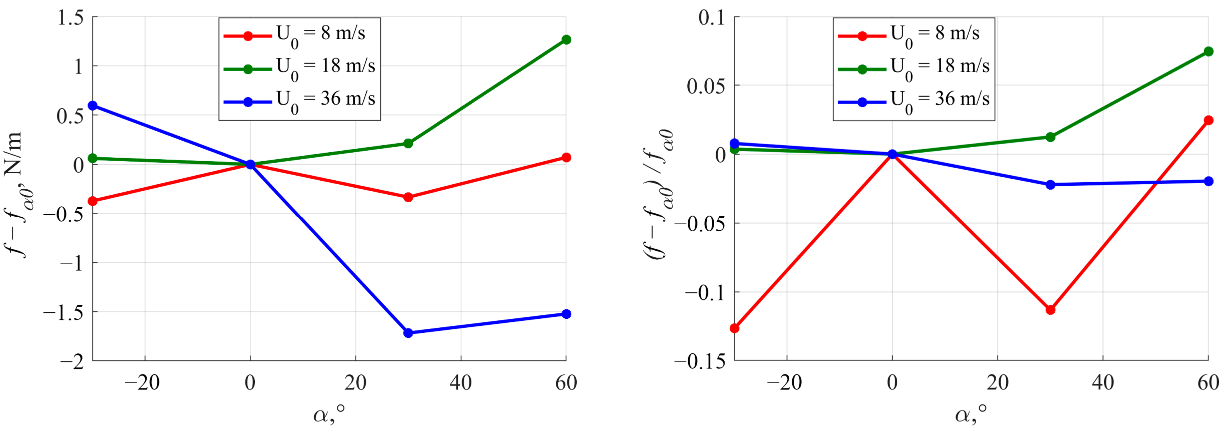

(**a**) (**b**)

Figure 15. Variation in the specific force estimated by Equation (1): (**a**)—absolute, (**b**)—relative.

The isolines of streamwise velocity corresponding to the range of $0.05 \leq U_X \leq 0.05$ m/s, and plotted to determine the position of the separation line, are shown in Figure 17. In a flow without MDA impact, the separation line was located at a distance of $X_s = 526$ mm. At the voltage amplitude $E = \pm 5$ kV, the separation shift was imperceptible. As the voltage amplitude increased, the jet character of the flow in the boundary layer became pronounced. This led to a significant separation line shift downstream to $X_s = 547$ mm at $E = \pm 7$ kV and to $X_s = 554$ mm at $E = \pm 8$ kV, as well as a simultaneous sharp increase in the reverse flow region. The separation structure changes dramatically.

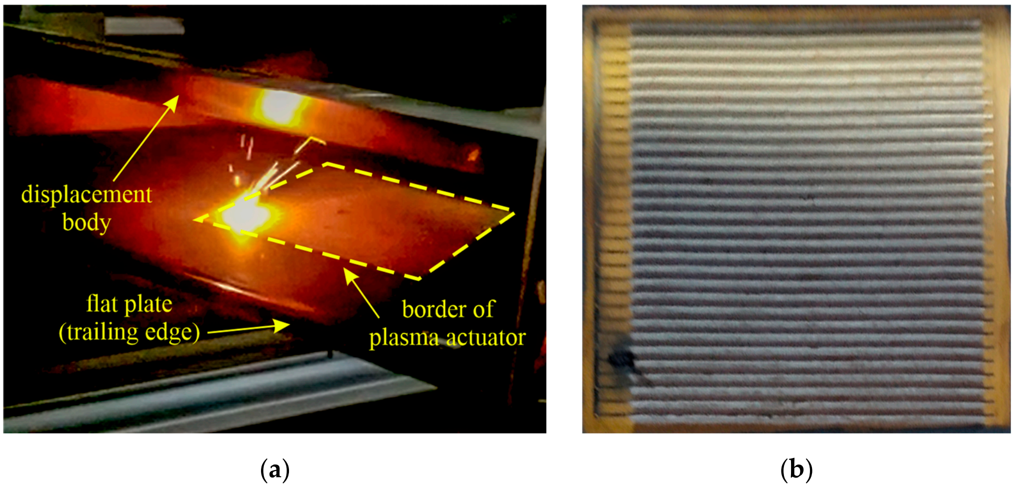

Figure 16. Electrical breakdown of MDA at voltage amplitude $E = \pm 8$ kV: (**a**)—photo of a burning MDA, (**b**)—look of the burnt-out MDA.

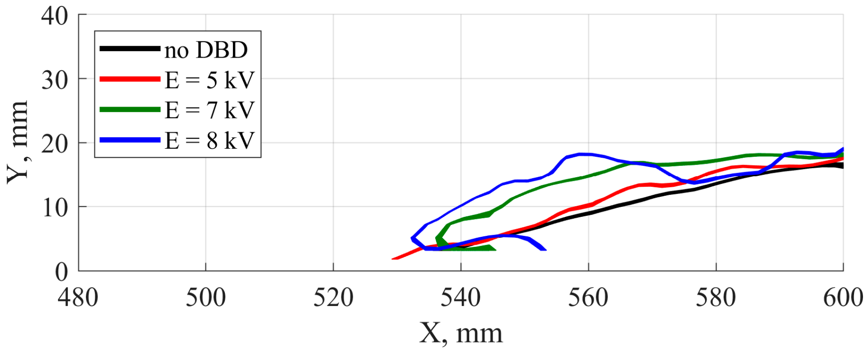

Figure 17. Isolines of streamwise velocity U_X at a free stream velocity of U_0 = 18 m/s and an MDA rotation angle of $\alpha = 0°$.

However, the favorable effect of the MDA, which is a decrease in the flow momentum loss, grew significantly with the increase in the voltage amplitude, which is shown in Figure 18. An increase in the amplitude of the voltage applied to the MDA led to a decrease in both pressure losses and the transverse size of the wake. Therefore, the viscous slat wake descended down to the flap model surface.

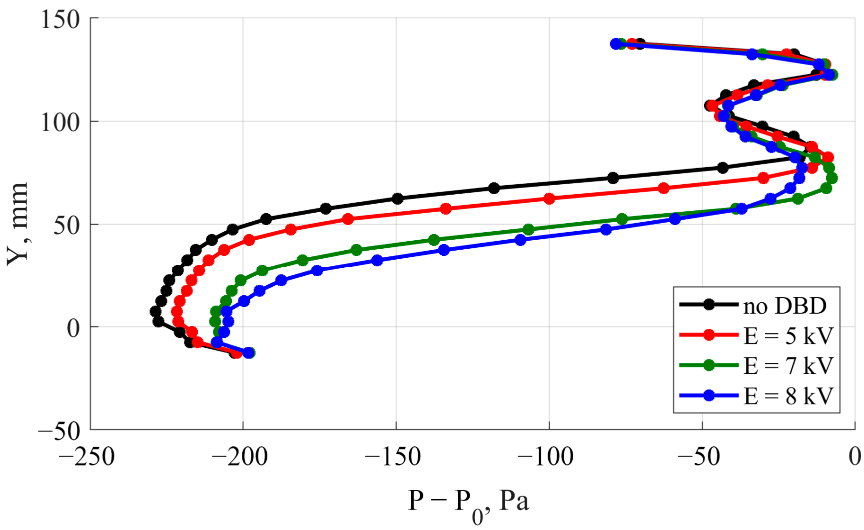

Figure 18. Total pressure losses in separation wake at U_0 = 18 m/s.

The decrease in the integral losses of the flow momentum, due to separation and friction, and the estimation of which was the specific force f (1) subject to the applied voltage, are shown in Figure 19, where $\Delta f = f - f_0$, f_0 is the value of the specific force (1) without the MDA impact. The decrease in the MDA efficiency at a voltage of $E = \pm 8$ kV compared to $E = \pm 7.5$ kV can, apparently, be explained by the discharge uniformity perturbation, as mentioned above.

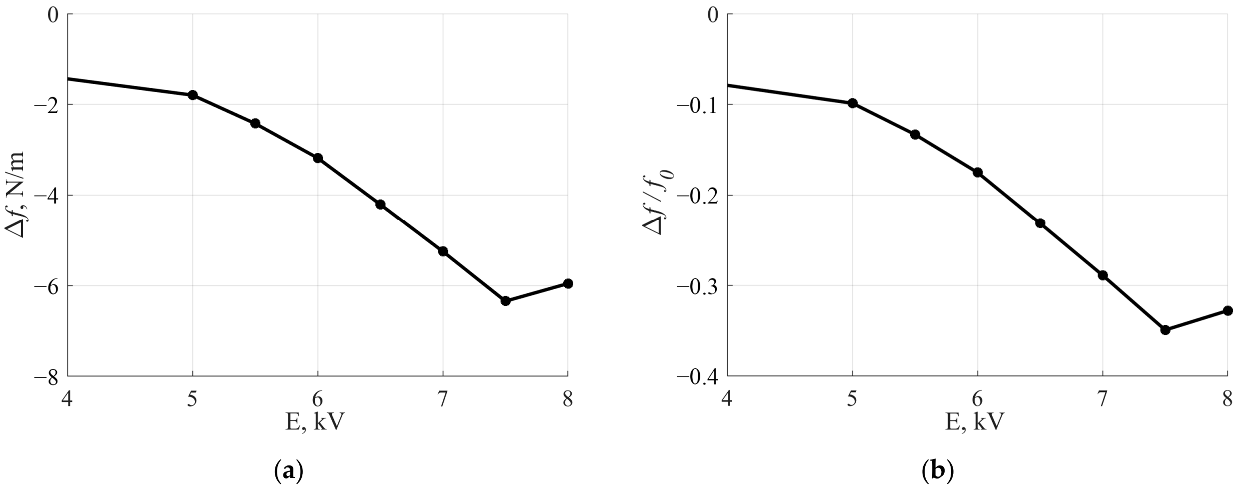

Figure 19. Variation in the total flow momentum losses subject to voltage amplitude: (**a**)—absolute, (**b**)—relative.

5. Conclusions

Using a multi-discharge plasma actuator, a unidirectional streamwise volume force effect on the flow was generated in the vicinity of the three-dimensional developed turbulent boundary layer separation region on the swept flap model. Based on PIV measurements of the flow structure, as well as measurements performed using a Pitot comb installed in the test model wake, the following new results were obtained.

When controlling a three-dimensional separation on a swept flap, it was proven that at a fixed velocity of the external flow and a fixed intensity of the MDA force impact, the result of this impact significantly depends on its direction. The greatest positive effects, namely, the separation line shift downstream, a decrease in the transverse size of the separation region, and a decrease in the total pressure loss in the wake, were observed at a positive angle between the direction of the volume force generated by the MDA and that perpendicular to the trailing edge of the model. In this configuration, the MDA force action led to an acceleration of the velocity components directed towards the trailing edge and along it. A similar effect was also observed at a negative angle between the volume force and that perpendicular to the edge, when the velocity component directed along the edge was decelerated by the MDA action. These results indicate the existence of an optimal force action direction, which may depend on both its intensity and the flow velocity.

Even with a slight shift of the three-dimensional separation line, which was observed at a high free stream velocity, as a result of the MDA action, the flow momentum losses due to friction forces and flow separation on the model were significantly reduced in the wake, and the transverse size of the wake decreased. The most unexpected result was as follows. At a high enough force, remarkably, the impact of the plasma actuator induced near-wall flow penetration downstream, but the separation region in its beginning strongly "swelled" and shifted upstream. Both the size of the viscous wake and the total pressure losses within it were reduced to the highest extent.

In further studies, we plan to use a multi-discharge actuator with increased thicknesses of the dielectric layers and greater distance between external electrodes, which will enhance the force effect and increase its vertical dimensions. In addition, the actuator will consist of three consecutive sections suitable for their independent connection to a power source. This will make it possible to separately study the effect of the force impact before the separation region in the vicinity of the separation line and behind the separation line, as well as their various combinations.

Author Contributions: Conceptualization, S.C., A.K. and D.S.; data curation, D.S. and S.T.; formal analysis, G.G., D.S. and S.T.; funding acquisition, S.C. and A.K.; investigation, G.G. and S.T.; methodology, G.G., A.K., D.S. and S.T.; project administration, S.C. and A.K.; resources, G.G. and S.T.; software, G.G., D.S. and S.T.; supervision, D.S.; visualization, D.S. and S.T.; writing—original draft, A.K., D.S. and S.T.; writing—review and editing, A.K., G.G., S.C., D.S. and S.T. All authors have read and agreed to the published version of the manuscript.

Funding: The article was prepared for the implementation of the program involving the creation and development of the World-Class Research Center "Supersonic" for 2020–2025, funded by the Ministry of Science and Higher Education of the Russian Federation (Grant Agreement of 17 May 2022, № 075-15-2022-1023).

Data Availability Statement: The data presented in the manuscript are available from the authors upon reasonable request.

Conflicts of Interest: The authors declare no conflict of interest. The funders had no role in the design of the study; in the collection, analyses, or interpretation of data; in the writing of the manuscript; or in the decision to publish the results.

References

1. Cattafesta, L.N.; Sheplak, M. Actuators for Active Flow Control. *Annu. Rev. Fluid Mech.* **2011**, *43*, 247–272. [CrossRef]
2. Enloe, C.L.; McLaughlin, T.E.; VanDyken, R.D.; Kachner, K.D.; Jumper, E.J.; Corke, T.C. Mechanisms and Responses of a Single Dielectric Barrier Plasma Actuator: Plasma Morphology. *AIAA J.* **2004**, *42*, 589–594. [CrossRef]
3. Moreau, E. Airflow Control by Non-Thermal Plasma Actuators. *J. Phys. D Appl. Phys.* **2007**, *40*, 605–636. [CrossRef]
4. Corke, T.C.; Post, M.L.; Orlov, D.M. SDBD Plasma Enhanced Aerodynamics: Concepts, Optimization and Applications. *Prog. Aerosp. Sci.* **2007**, *43*, 193–217. [CrossRef]
5. Corke, T.C.; Enloe, C.L.; Wilkinson, S.P. Dielectric Barrier Discharge Plasma Actuators for Flow Control. *Annu. Rev. Fluid Mech.* **2010**, *42*, 505–529. [CrossRef]
6. Wang, J.-J.; Choi, K.-S.; Feng, L.-H.; Jukes, T.N.; Whalley, R.D. Recent Developments in DBD Plasma Flow Control. *Prog. Aerosp. Sci.* **2013**, *62*, 52–78. [CrossRef]
7. Benard, N.; Moreau, E. Electrical and Mechanical Characteristics of Surface AC Dielectric Barrier Discharge Plasma Actuators Applied to Airflow Control. *Exp. Fluids* **2014**, *55*, 1846. [CrossRef]
8. Kriegseis, J.; Simon, B.; Grundmann, S. Towards In-Flight Applications? A Review on Dielectric Barrier Discharge-Based Boundary-Layer Control. *Appl. Mech. Rev.* **2016**, *68*, 020802. [CrossRef]
9. Corke, T.C.; Bowles, P.O.; He, C.; Matlis, E.H. Sensing and Control of Flow Separation Using Plasma Actuators. *Philos. Trans. R. Soc. A* **2011**, *369*, 1459–1475. [CrossRef]
10. Roth, J.R.; Sherman, D.M.; Wilkinson, S.P. Electrohydrodynamic Flow Control with a Glow-Discharge Surface Plasma. *AIAA J.* **2000**, *38*, 1166–1172. [CrossRef]
11. Sato, M.; Okada, K.; Asada, K.; Aono, H.; Nonomura, T.; Fujii, K. Unified Mechanisms for Separation Control around Airfoil Using Plasma Actuator with Burst Actuation over Reynolds Number Range of 103–106. *Phys. Fluids* **2020**, *32*, 025102. [CrossRef]
12. Maslov, A.; Sidorenko, A.; Zanin, B.; Postnikov, B.; Budovsky, A.; Malmuth, N. Plasma Control of Flow Separation on Swept Wing at High Angles of Attack. In Proceedings of the 46th AIAA Aerospace Sciences Meeting and Exhibit, Reno, NV, USA, 7 January 2008; American Institute of Aeronautics and Astronautics: Reno, NV, USA, 2008.
13. Kato, K.; Breitsamter, C.; Obi, S. Flow Control over Swept Wings Using Nanosecond-Pulse Plasma Actuator. *Int. J. Heat Fluid Flow* **2016**, *61*, 58–67. [CrossRef]
14. Kato, K.; Breitsamter, C.; Obi, S. Flow Separation Control over a Gö 387 Airfoil by Nanosecond Pulse-Periodic Discharge. *Exp. Fluids* **2014**, *55*, 1795. [CrossRef]
15. Zhao, G.; Li, Y.; Liang, H.; Han, M.; Wu, Y. Flow Separation Control on Swept Wing with Nanosecond Pulse Driven DBD Plasma Actuators. *Chin. J. Aeronaut.* **2015**, *28*, 368–376. [CrossRef]
16. Zhang, X.; Huang, Y.; Wang, X.; Wang, W.; Tang, K.; Li, H. Turbulent Boundary Layer Separation Control Using Plasma Actuator at Reynolds Number 2000000. *Chin. J. Aeronaut.* **2016**, *29*, 1237–1246. [CrossRef]
17. Nelson, R.; Corke, T.; Othman, H.; Patel, M.; Vasudevan, S.; Ng, T. A Smart Wind Turbine Blade Using Distributed Plasma Actuators for Improved Performance. In Proceedings of the 46th AIAA Aerospace Sciences Meeting and Exhibit, Reno, NV, USA, 7 January 2008; American Institute of Aeronautics and Astronautics: Reno, NV, USA, 2008.
18. Benard, N.; Mizuno, A.; Moreau, E. A Large-Scale Multiple Dielectric Barrier Discharge Actuator Based on an Innovative Three-Electrode Design. *J. Phys. D Appl. Phys.* **2009**, *42*, 235204. [CrossRef]

19. Berendt, A.; Podliński, J.; Mizeraczyk, J. Multi-DBD Actuator with Floating Interelectrode for Aerodynamic Control. *Nukleonika* **2012**, *57*, 249–252.
20. Debien, A.; Benard, N.; Moreau, E. Streamer Inhibition for Improving Force and Electric Wind Produced by DBD Actuators. *J. Phys. D Appl. Phys.* **2012**, *45*, 215201. [CrossRef]
21. Hao, J.; Tian, B.; Wang, Y.; Song, Y.; Pan, S.; Li, W. Dielectric Barrier Plasma Dynamics for Active Aerodynamic Flow Control. *Sci. China Phys. Mech. Astron.* **2014**, *57*, 345–353. [CrossRef]
22. Sato, S.; Ozawa, Y.; Komuro, A.; Nonomura, T.; Asai, K.; Ohnishi, N. Experimental Demonstration of Low-Voltage Operated Dielectric Barrier Discharge Plasma Actuators Using SiC MOSFETs. *J. Phys. D Appl. Phys.* **2020**, *53*, 43LT01. [CrossRef]
23. Gamirullin, M.D.; Kuryachii, A.P.; Litvinov, V.M.; Chernyshev, S.L. Investigation of a Simplified Scheme of Multiple Plasma Actuator for Boundary Layer Control. *TsAGI Sci. J.* **2014**, *45*, 889–901. [CrossRef]
24. Chernyshev, S.L.; Gamirullin, M.D.; Kuryachii, A.P.; Litvinov, V.M. Simple Design of Multiple Aerodynamic Plasma Actuator. In *Proceedings of the Progress in Flight Physics*; Knight, D., Bondar, Y., Lipatov, I., Reijasse, P., Eds.; EDP Sciences: Krakow, Poland, 2017; pp. 253–264.
25. Baranov, S.A.; Chernyshev, S.L.; Khomich, V.Y.; Kiselev, A.P.; Kuryachii, A.P.; Moshkunov, S.I.; Rebrov, I.E.; Sboev, D.S.; Tolkachev, S.N.; Yamshchikov, V.A. Experimental Cross-Flow Control in a 3D Boundary Layer by Multi-Discharge Plasma Actuators. *Aerosp. Sci. Technol.* **2021**, *112*, 106643. [CrossRef]
26. Van Den Berg, B.; Elsenaar, A.; Lindhout, J.P.F.; Wesseling, P. Measurements in an Incompressible Three-Dimensional Turbulent Boundary Layer, under Infinite Swept-Wing Conditions, and Comparison with Theory. *J. Fluid Mech.* **1975**, *70*, 127–148. [CrossRef]
27. Zanin, B.Y.; Kozlov, V.V.; Pavlenko, A.M. Control of Flow Separation from a Model Wing at Low Reynolds Numbers. *Fluid Dyn.* **2012**, *47*, 403–410. [CrossRef]
28. Clauser, F.H. Turbulent Boundary Layers in Adverse Pressure Gradients. *J. Aeronaut. Sci.* **1954**, *21*, 91–108. [CrossRef]